ELSEVIER

Journal of Hazardous Materials A108 (2004) 9–20

Journal of Hazardous Materials

www.elsevier.com/locate/jhazmat

Validation of turbulence models in heavy gas dispersion over obstacles

Spyros Sklavounos, Fotis Rigas*

School of Chemical Engineering, National Technical University of Athens, 15700 Athens, Greece

Received 16 October 2003; received in revised form 19 December 2003; accepted 22 January 2004

Abstract

Accidental release and dispersion of toxic gases were always major hazards for public health and safety that process industries had to deal with. Real terrain dispersion simulation for risk analysis purposes poses specific difficulties related to complex turbulence phenomena development, especially when obstructions are found into the flow region. In this paper, several turbulence models are tested and compared against experimental data of dense vapor dispersion, in order to decide for their suitability for simulating such flows. Computations were carried out using the computational fluid dynamics (CFD) code CFX 5.6, while experimental data were obtained from Thorney Island large scale field trials. Computational results showed good agreement with experimental measurements indicating that CFDs provide a reliable means of estimating gas dispersion in real terrains.

Keywords: Heavy gas; Dispersion simulation; Turbulence modeling; CFD; Complex terrain; Obstructed flow

1. Introduction

Atmospheric dispersion of hazardous (toxic, flammable) gases and vapors constitutes a severe threat for populations adjacent to industries and storage areas, where such materials are handled. Quantitative risk analysis for loss prevention purposes demands successful simulation of eventual accidental events, which is usually implemented with empirical models. Another way is the use of advanced techniques offered by computational fluid dynamics tools, which provide a more precise and analytical approach to the studied phenomenon.

With reference to gas dispersion, the so-called box models developed in the past (SLAB, DEGADIS) are widely used in risk analysis procedures providing relatively easy and fast dispersion estimations [1,2]. Despite the convenience they offer in their application, they appear to have some major drawbacks: they describe unobstructed gas flow in flat terrains and therefore cannot correctly model the physics of complex interactions between scattered gas and obstacles. Furthermore, they are one-dimensional averaging gas properties in the two dimensions vertical to dispersion direction [3]. In fact, the properties of dispersed gas change in three dimensions, whereas risk estimation for inhabited areas imposes the presence of obstacles (buildings) within the flow field. Moreover, the prediction of turbulent mixing between scattering gas and air particles demands the use of specific turbulent models.

On the other hand, computational fluid dynamics allows the simulation of complex physical processes describing heat and mass transport phenomena with fully developed mathematical models. Specific models incorporated in CFD codes predict the turbulent mixing between gas molecules and air particles, in addition to cavity regions in the flow field (building wakes), which may result in entrapment of escaping gas at low heights for relatively long time with increased health effects.

Numerical simulation of dense gas dispersions have been carried out in the past [4,5] using k–ε turbulence model with encouraging results. In this paper, k–ε in addition to three other newly developed turbulence models (k–ω, shear stress transport and SSG Reynolds) are tested against Thorney Island field trials data. Thorney Island experiments are well documented and analyzed in depth in the relevant bibliography [6–8] providing useful information for subsequent dense gas experiments set-up [9] and constituting a reliable data set that have been used in verification procedures of box [10] or more complicated [11–14] dispersion models.

Numerical simulation of the trials was performed via the use of CFX 5.6 code, which uses the Reynolds averaged

* Corresponding author. Fax: +30-1-07723267.
E-mail address: rigasf@central.ntua.gr (F. Rigas).

0304-3894/$ – see front matter © 2004 Elsevier B.V. All rights reserved.
doi:10.1016/j.jhazmat.2004.01.005

Nomenclature

C	constant (dimensionless)
$C_{\varepsilon 1}$	k–ε turbulence model unitless constant equal to 1.44
$C_{\varepsilon 2}$	k–ε turbulence model unitless constant equal to 1.92
C_μ	k–ε turbulence model unitless constant equal to 0.09
G	buoyancy production term of Reynolds stresses in SSG model ($kg\,m^{-1}\,s^{-3}$)
k	turbulence kinetic energy per unit mass ($m^2\,s^{-2}$)
m_i	constant mass inflow rate ($kg\,s^{-1}$)
p	static (thermodynamic) pressure ($kg\,m^{-1}\,s^{-2}$)
p'	modified pressure ($kg\,m^{-1}\,s^{-2}$)
P	shear production term of the Reynolds stresses in SSG model ($kg\,m^{-1}\,s^{-3}$)
P_k	production rate of turbulence ($kg\,m^{-1}\,s^{-3}$)
P_{kb}	buoyancy production term ($kg\,m^{-1}\,s^{-3}$)
Q_i	variable mass inflow rate equal to m_i during the release phase ($kg\,s^{-1}$)
S_φ	source term of scalar variable φ
t	time (s)
t_c	time constant equal to 1 s
t_0	time of release initiation (s)
t_1	release phase duration (s)
u	fluctuating velocity component in turbulent flow ($m\,s^{-1}$)
u_z	wind speed at height z ($m\,s^{-1}$)
u_0	wind speed at 10 m height ($m\,s^{-1}$)
U	velocity vector ($m\,s^{-1}$)
Z	vertical coordinate (m)
Z_0	reference height equal to 10 m

Greek letters

α_1	dimensionless constant
Γ	dynamic diffusivity ($kg\,m^{-1}\,s^{-1}$)
δ	the identity matrix/Kronecker delta function
ε	turbulence eddy dissipation rate ($m^2\,s^{-3}$)
ζ	bulk viscosity ($kg\,m^{-1}\,s^{-1}$)
λ	dimensionless parameter
μ	molecular (dynamic) viscosity ($kg\,m^{-1}\,s^{-1}$)
μ_{eff}	effective viscosity accounting for turbulence, $\mu + \mu_t$ ($kg\,m^{-1}\,s^{-1}$)
μ_t	turbulence dynamic viscosity ($kg\,m^{-1}\,s^{-1}$)
ν_t	turbulence kinematic viscosity ($m^2\,s^{-1}$)
π	experimental value of gas cloud arrival time (s) or concentration (%, v/v)
ρ	density ($kg\,m^{-3}$)
σ_k	dimensionless turbulence model constant for the k equation equal to 1.0
σ_ε	dimensionless constant in the k–ε turbulence model equal to 1.3
σ_ω	dimensionless constant in the k–ω turbulence model equal to 1.3
τ	shear stress/molecular stress tensor ($kg\,m^{-1}\,s^{-2}$)
υ	computational value of gas cloud arrival time (s) or concentration (%, v/v)
Φ	pressure strain tensor
φ	general scalar variable
ω	turbulent frequency (s^{-1})

Subscript

i	ith trial

Superscript

T	transpose of matrix

Navier–Stokes equations and is based on the finite volume method for the governing equations discretization, namely, the conversion of partial differential equations and auxiliary (boundary and initial) conditions into a discrete system of algebraic equations [15]. Comparisons between simulation results and experimental data show good agreement between them, resulting in the conclusion that advanced computational fluid dynamics techniques can be successfully applied in risk analysis procedures with satisfactory accuracy.

2. CFD code structure

CFD codes are usually divided into three parts: preprocessor, solver and post-processor for problem definition, problem solution and results processing, respectively. CFX 5.6 code consists of four subsequent parts (Fig. 1):

1. CFX-Build, in which the computational domain geometry is constructed by the use of PATRAN Command Language (PCL). Moreover, the division of the main domain into a number of smaller control volumes (mesh generation) is achieved in this step.
2. CFX-Physics processor, where boundary conditions, turbulence models, domain fluids and solution scheme are defined.
3. CFX-Solver, where the code performs calculations towards the final solution until the desired accuracy is achieved.
4. CFX-Post, in which the elaboration of the results takes place, supported by outstanding graphics capabilities (visualization of the geometry and control volumes, vector plots showing the direction and magnitude of the flow, visualization of the variation of scalar variables through the domain). Quantitative numerical calculations are also performed in this stage.

In CFX-Build, after the desired geometry has been defined, the entire domain is sub-divided into a number of

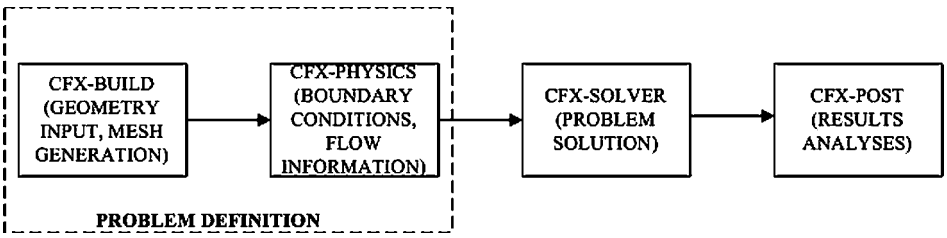

Fig. 1. The four stages in a CFD simulation.

smaller sub-domains (control volumes or cells) forming a mesh, through the grid generation process (step 1). Once the physical models which are to be included in the simulation have been selected and fluid(s) properties plus the boundary conditions have been entered (step 2), governing partial differential equations are integrated over all the control volumes and the integral equations are converted to a system of algebraic equations. The latter are solved iteratively at nodal points inside each cell aiming at minimization of the residuals (iteration loop error) until the prescribed convergence criteria are satisfied (step 3). In step 4, CFX-Post allows visualization and quantitative post-processing of CFD simulations results; it is capable of generating a large variety of graphical and geometric objects (points, lines, planes, volumes, isosurfaces, vectors, contours, streamlines) and calculating the values of certain user-specified variables on them.

As mentioned above, CFX code uses Reynolds averaged Navier–Stokes equations. The turbulence eddy frequency of the large eddies has been plotted in Fig. 2. The frequency is of the order of 1 Hz for most of the domain, so the time scale of the large eddies is of the order of 1 s. The experimental time needed for the measured escaping gas concentrations to dilute is of the order of 10–20 s. Thus, the transient phenomenon studied is slower than the time scale of large eddies and RANS averaging applies. Consequently, the experimental and numerical results are comparable.

3. Turbulence modeling

Turbulent flow can be defined as the viscous flow in which fluid particles move in a random and chaotic way within the flow field. The designation of viscous flow refers to the flow of a real fluid regardless of its viscosity value. Velocity and all other fluid properties vary continuously, with strong concurrent molecular mixing between adjacent fluid layers. In atmospheric flows, turbulence is the dominant mechanism in the mixing and dilution of gaseous releases [16], associated with the presence of natural obstacles (i.e. trees), human structures (i.e. buildings) and ground surface roughness.

Specific models are used to predict such effects in complex fluid flows, where the presence of turbulence is certain. Some have limited applications, while others can be applied to a wider class of flows with a reasonable degree of confidence. Most of them have been based on the Reynolds averaged Navier–Stokes (RANS) equations [17] and can be classified as either eddy-viscosity or Reynolds stress models.

Eddy-viscosity turbulence models suggest that turbulence consists of small eddies which are continuously forming and dissipating, and in which the Reynolds stresses are assumed to be proportional to mean velocity gradients. The simple zero-equation model plus to the more complex two-equation turbulence models comprise the family of eddy-viscosity models.

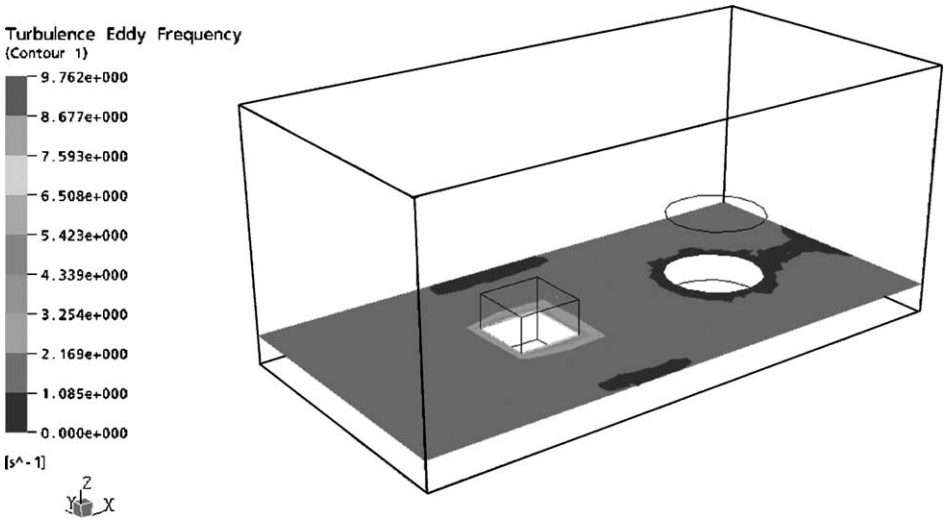

Fig. 2. Turbulence eddy frequency (s^{-1}) of large eddies in the computational domain.

The Reynolds stress models are based on transport equations for all components of the Reynolds stress tensor and the dissipation rate. The inherent modeling of stress anisotropies theoretically makes Reynolds stress models more suited to complex flows, practice, however, shows that they are often not better than the two-equation models.

Four turbulence models were tested in this work for their ability to predict the atmospheric dispersion of gas releases: k–ε (standard), k–ω (standard), SST and SSG Reynolds stress. A brief discussion and the theoretical background for each model follow in the next paragraphs.

3.1. k–ε model

Belonging to the family of eddy-viscosity models, this is one of the most prominent turbulence prediction tools implemented in many general purpose CFD codes. It has proven to be stable and numerically robust having a well established predictive capability. The k–ε model uses the scalable wall-function approach instead of standard wall functions, improving robustness and accuracy when the near-wall mesh is very fine.

The k–ε model introduces two new variables into the system of conservation equations, which take the form [18,19]:

- Continuity equation:

$$\frac{\partial \rho}{\partial t} + \nabla(\rho U) = 0 \tag{3.1}$$

- Momentum equation:

$$\frac{\partial \rho U}{\partial t} + \nabla(\rho U \otimes U) - \nabla(\mu_{\text{eff}} \nabla U) = \nabla p' + \nabla(\mu_{\text{eff}} \nabla U)^{\text{T}} + B \tag{3.2}$$

where B is the sum of body forces and p' the modified pressure given by

$$p' = p + \tfrac{2}{3}\rho k \tag{3.3}$$

and

$$\mu_{\text{eff}} = \mu + \mu_{\text{t}} \tag{3.4}$$

The k–ε model assumes that the turbulence viscosity is linked to the turbulence kinetic energy and dissipation via the relation

$$\mu_{\text{t}} = \frac{C_\mu \rho k^2}{\varepsilon} \tag{3.5}$$

The values of k and ε are directly calculated from the differential transport equations for the turbulence kinetic energy and turbulence dissipation rate

$$\frac{\partial(\rho k)}{\partial t} + \nabla(\rho U k) = \nabla\left[\left(\mu + \frac{\mu_{\text{t}}}{\sigma_k}\right)\nabla k\right] + P_k - \rho\varepsilon \tag{3.6}$$

$$\frac{\partial(\rho \varepsilon)}{\partial t} + \nabla(\rho U \varepsilon) = \nabla\left[\left(\mu + \frac{\mu_{\text{t}}}{\sigma_\varepsilon}\right)\nabla \varepsilon\right] + \frac{\varepsilon}{k}(C_{\varepsilon 1} P_k - C_{\varepsilon 2}\rho\varepsilon) \tag{3.7}$$

where P_k is the turbulence production due to viscous and buoyancy forces, which is modeled using

$$P_k = \mu_{\text{t}} \nabla U(\nabla U + \nabla U^{\text{T}}) - \tfrac{2}{3}(\nabla U)(3\mu_{\text{t}}\nabla U + \rho k) + P_{k\text{b}} \tag{3.8}$$

3.2. k–ω and SST model

One of the main problems in turbulence modeling is the accurate prediction of flow separation from a smooth surface, existing in many technical applications both for external and internal flows. Models based on the ε-equation predict the onset of separation too late and under-predict the amount of separation later on. Currently, the outstanding eddy-viscosity models in this area are the k–ε based models. SST (shear stress transport) model was developed to overcome deficiencies in the standard k–ω model and it is considered more integrated compared with k–ω and is recommended for high accuracy boundary layer simulation. Both k–ω and SST belong to eddy-dissipation models.

The k–ω model assumes that the turbulence viscosity is linked to the turbulence kinetic energy and turbulent frequency via the relation

$$\mu_{\text{t}} = \frac{\rho k}{\omega} \tag{3.9}$$

It solves two transport equations, one for the turbulent kinetic energy k and one for the turbulent frequency ω:

- k-equation:

$$\frac{\partial(\rho k)}{\partial t} + \nabla(\rho U k) = \nabla\left[\left(\mu + \frac{\mu_{\text{t}}}{\sigma_k}\right)\nabla k\right] + P_k - \beta'\rho k\omega \tag{3.10}$$

- ω-equation:

$$\frac{\partial(\rho \omega)}{\partial t} + \nabla(\rho U \omega) = \nabla\left[\left(\mu + \frac{\mu_{\text{t}}}{\sigma_\omega}\right)\nabla \omega\right] + \frac{\alpha\omega P_k}{k} - \beta\rho\omega^2 \tag{3.11}$$

P_k is the production rate of turbulence, which is calculated as in the k–ε model (Eq. (3.8)). The model constants are given by

$$\beta' = 0.09, \quad \alpha = \tfrac{5}{9}, \quad \beta = 0.075, \quad \sigma_k = \sigma_\omega = 2 \tag{3.12}$$

Both k–ε and k–ω turbulence models do not account for the transport of the turbulent shear stress resulting in an overprediction of the eddy-viscosity. The proper transport behavior can be obtained by a limiter to the formulation of the eddy-viscosity:

$$\nu_{\text{t}} = \frac{\alpha_1 k}{\max(\alpha_1 \omega, SF)} \tag{3.13}$$

where

$$\nu_{\text{t}} = \frac{\mu_{\text{t}}}{\rho} \tag{3.14}$$

F is a blending function of the distance to the nearest wall and the flow variables k, ω, which restricts the limiter to the wall boundary layer, while S is an invariant measure of the strain rate.

3.3. SSG Reynolds stress model

Reynolds stress models have shown superior predictive performance compared to eddy-viscosity models in cases, such as buoyant flows or free shear flows with strong anisotropy. These models are based on transport equations for all components of the Reynolds stress tensor and the dissipation rate.

SSG model solves differential transport equations individually for each Reynolds stress component and therefore is a differential Reynolds stress model (discriminated from algebraic models that solve algebraic equations).

Although Reynolds stress models are generally flexible, the increased number of transport equations leads to a higher degree of complexity, and thus reduced robustness and increased computational effort.

The Reynolds averaged momentum and Reynolds stresses transport equations are listed below:

- Reynolds averaged momentum equation:

$$\frac{\partial(\rho U)}{\partial t} + \nabla(\rho U \otimes U) - \nabla(\mu \nabla U) = -\nabla p'' - \nabla(\rho \overline{u \otimes u}) + B \tag{3.15}$$

where p'' is a modified pressure related to the static (thermodynamic) pressure by

$$p'' = p + \nabla U \left(\frac{2\mu}{3} - \zeta\right) \tag{3.16}$$

- Reynolds stresses differential transport equation:

$$\frac{\partial(\rho \otimes u)}{\partial t} + \nabla(\rho \overline{u \otimes u} \otimes U) - \nabla\left[\rho C \left(\frac{k}{\varepsilon}\right) \overline{u \otimes u} (\nabla \overline{u \otimes u})^{\mathrm{T}}\right] = P + G + \Phi - \frac{2}{3}\rho\varepsilon\delta \tag{3.17}$$

where P and G are the shear and buoyancy turbulence production terms of the Reynolds stresses, respectively, Φ the pressure strain tensor and C is a constant.

3.4. Introduction to CFX-Solver theory

Analytical solutions to the Navier–Stokes equations exist for only the simplest of flows under ideal conditions. To obtain solutions for real flows a numerical approach must be adopted whereby the equations are replaced by algebraic approximations which may be solved using a numerical method [17,19].

3.4.1. Discretization of the governing equations

This approach involves discretizing the spatial domain into finite control volumes using a mesh. The governing equations are integrated over each control volume, such that the relevant quantity (mass, momentum, energy, etc.) is conserved in a discrete sense for each control volume. Consider the mean form of the conservation equations for mass, momentum and energy, expressed in Cartesian coordinates:

$$\frac{\partial \rho}{\partial t} + \frac{\partial(\rho U_j)}{\partial x_j} = 0 \tag{3.18}$$

$$\frac{\partial(\rho U_i)}{\partial t} + \frac{\partial(\rho \mu_j U_i)}{\partial x_j} = -\frac{\partial p}{\partial x_i} + \frac{\partial[\mu_{\mathrm{eff}}(\partial U_i/\partial x_j + \partial U_j/\partial x_i)]}{\partial x_j} \tag{3.19}$$

$$\frac{\partial(\rho\phi)}{\partial t} + \frac{\partial(\rho \mu_j \phi)}{\partial x_j} = \frac{\partial[T(\partial\varphi/\partial x_j)]}{\partial x_j} + S_\varphi \tag{3.20}$$

These equations can be integrated over a fixed control volume, using Gauss' divergence theorem to convert volume integrals to surface integrals as follows:

$$\frac{\partial\left[\int_v \rho \,\mathrm{d}v\right]}{\partial t} + \int_s \rho U_j \,\mathrm{d}n_j = 0 \tag{3.21}$$

$$\frac{\partial\left[\int_v \rho U_i \,\mathrm{d}v\right]}{\partial t} + \int_s \rho U_j U_i \,\mathrm{d}n_j = -\int_s P \,\mathrm{d}n_j + \int_s \mu_{\mathrm{eff}} \left[\left(\frac{\partial U_i}{\partial x_j}\right) + \left(\frac{\partial U_j}{\partial x_i}\right)\right] \mathrm{d}n_j + \int_v S_{U_i} \,\mathrm{d}v \tag{3.22}$$

$$\frac{\partial\left[\int_v \rho\phi \,\mathrm{d}v\right]}{\partial t} + \int_s \rho U_j \phi \,\mathrm{d}n_j = \int_s \Gamma \left(\frac{\partial\varphi}{\partial x_j}\right) \mathrm{d}n_j + \int_v S_\phi \,\mathrm{d}v \tag{3.23}$$

where v and s denote volume and surface integrals, respectively, and $\mathrm{d}n_j$ are the differential Cartesian components of the outward normal surface vector. The surface integrals are the integrations of the fluxes, whereas the volume integrals represent source or accumulation terms.

The first step in solving these continuous equations numerically is to approximate them using discrete functions. The surface fluxes must be discretely represented at the integration points to complete the conversion of the continuous equation into their discrete form. The integration points, ip_n, are located at the center of each surface segment in a 3D element surrounding the finite volume:

$$\frac{\rho V(\rho - \rho^{\mathrm{o}})}{\Delta t} + \sum_{\mathrm{ip}} (\rho U_j \,\Delta n_j)_{\mathrm{ip}} = 0 \tag{3.24}$$

$$\frac{\rho V(U_i - U_i^{\mathrm{o}})}{\Delta t} + \sum_{\mathrm{ip}} \dot{m}_{\mathrm{ip}}(U_i)_{\mathrm{ip}} = \sum_{\mathrm{ip}} (P\,\Delta n_i)_{\mathrm{ip}} + \sum_{\mathrm{ip}} \left[\mu_{\mathrm{eff}} \left[\left(\frac{\partial U_i}{\partial x_j} \right) + \left(\frac{\partial U_j}{\partial x_i} \right) \right] \Delta n_j \right]_{\mathrm{ip}} + \overline{S_{U_i}} V \tag{3.25}$$

$$\frac{\rho V(\varphi - \varphi^{\mathrm{o}})}{\Delta t} + \sum_{\mathrm{ip}} \dot{m}_{\mathrm{ip}} \phi_{\mathrm{ip}} = \sum_{\mathrm{ip}} \left[\Gamma \left(\frac{\partial \phi}{\partial x_j} \right) \Delta n_j \right]_{\mathrm{ip}} + \overline{S_\phi} V \tag{3.26}$$

where V is the control volume, the subscript ip denotes an integration point, the summation is over all the integration points of the finite volume, Δn_j the discrete outward surface vector and Δt the time step. Note that the first-order backward Euler scheme has been assumed in this equation, and the same solution scheme was used during the simulation of the trials.

Superscript o refers to the old time level. The discrete mass flow through a surface of the finite volume is denoted by $\dot{m}_{\mathrm{ip}}$ and is given by

$$\dot{m}_{\mathrm{ip}} = (\rho U_j\,\Delta n_j)^{\mathrm{o}}_{\mathrm{ip}} \tag{3.27}$$

When the solution for a non-steady state problem is meant, the first-order backward Euler scheme approximates the transient term as

$$\frac{\partial \left[\int_v \rho\phi \,\mathrm{d}v \right]}{\partial t} = \frac{\rho V(\varphi - \varphi^{\mathrm{o}})}{\Delta t} \tag{3.28}$$

3.4.2. The coupled system of equations

The linear set of equations that arise by applying the finite volume method to all elements in the domain are discrete conservation equations. The system of equations can be written in the form

$$\sum_{\mathrm{nb}_i} a_i^{\mathrm{nb}} \phi_i = b_i \tag{3.29}$$

where φ is the solution, b the right-hand side, a the coefficients of the equation, i the identifying number of the finite volume or node in question, and nb the "neighbor", but also includes the central coefficient multiplying the solution at the ith location. The node may have any number of such neighbors, so that the method is equally applicable to both structured and unstructured meshes. The set of these for all finite volumes constitutes the whole linear equation system.

3.4.3. Linear equation solution

The linearized system of discrete equations described above can be written in the general matrix form

$$[A][\varphi] = [b] \tag{3.30}$$

where $[A]$ is the coefficient matrix, $[\varphi]$ the solution vector and $[b]$ the right-hand side.

The above equation can be solved iteratively by starting with an approximate solution, φ^n, that is to be improved by a correction, φ', to yield a better solution, φ^{n+1}, i.e.

$$\varphi^{n+1} = \varphi^n + \varphi' \tag{3.31}$$

where φ' is a solution of

$$\dot{A}\varphi' = r^n \tag{3.32}$$

with r^n, the residual, obtained from

$$r^n = b - A\varphi^n \tag{3.33}$$

Repeated application of this algorithm will yield a solution of the desired accuracy.

4. Description of the Thorney Island field trials considered

In contrast with Phase I dense vapor dispersion trials at Thorney Island, where released gas was allowed to disperse in a flat site, the objective of Phase II was to study the dispersion of heavier than air gases around obstacles. Phase II program would generate a satisfactory set of results for validation of wind tunnel modeling schemes. Moreover, fluid dynamic phenomena such as the interaction between the density-stratified flow and the building (whether the gas flows around or over it) and the interaction between the wake of the building and the flow (turbulence enhancement) could also be investigated.

In the trials with the isolated building (nos. 26 and 29), the obstacle was a cube 9 m × 9 m × 9 m consisted of plastic sheets attached to a wooden frame. The complete structure was mounted on a trailer and was moved to the required position shortly before the release of gas, according to the wind direction record. The gas source was a cylindrical (actually 12-sided) tent of 14 m diameter, 13 m height and total volume capacity of 2000 m^3, made from flexible material, which was left to fall to the ground at the beginning of each trial [20].

4.1. Thorney Island trial no. 26

In this trial, the mobile cubical building was situated 50 m downwind from the cylindrical gas tent (Fig. 3) and the released gas was a mixture of Refrigerant-12 diluted with nitrogen. The percent gaseous mixture composition was 68.4% nitrogen and 31.6% Freon 12 (w/w). During the trial execution, wind speed was relatively low (1.9 $\mathrm{m\,s^{-1}}$) and the cloud was swept around the sides of the building without significant elevation at the front of the cube. However, the view from an elevated video camera showed that the cloud front splashed up the downwind building face. Concentration measurements were recorded on the front plus to the rear face of the obstacle (with respect to wind direction).

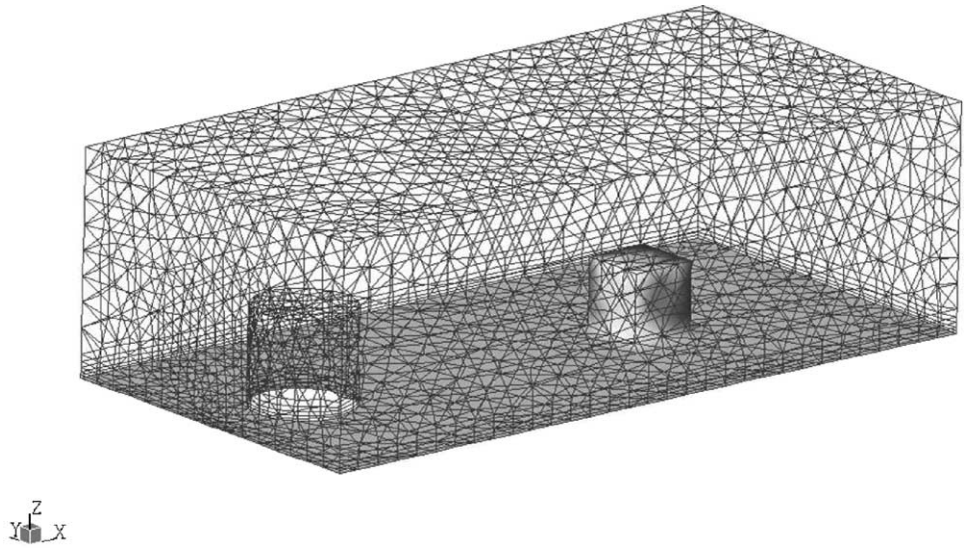

Fig. 3. Surface mesh of trial no. 26 computational domain. Air inflow from the left-hand side.

4.2. Thorney Island trial no. 29

This was the only trial performed with the building upwind from the gas source (Fig. 4). The gas released in this experiment was the same with that of trial no. 26 mixture, but the wind speed was relatively high (5.6 m s^{-1}). The separation from the rear face edge of the cube to the upwind surface edge of the source container was 20 m. Results obtained showed that the gravity front traveling upwind was entrained by the low pressure region in the wake of the building, resulting in gas entry into the wake and drawing up the rear face of the building. Very little gas was observed to travel around the sides of the obstacle, while available concentration measurements are referred to the rear face of the building [21].

5. Boundary conditions

Boundary conditions are specifications of properties or conditions on the surfaces of the domains and are required to fully define the flow simulation. Regarding the computational domains in Figs. 3 and 4, the boundary conditions set for the wind profile and gas inflow are demonstrated below.

5.1. Gas inflow

At Thorney Island nos. 26 and 29 tests, approximately 2000 m^3 of Freon 12/nitrogen mixture was released into the atmosphere in about 1.5 s [6], corresponding to an instantaneous release. In order to set the inflow boundary condition for the transient problem, released mixture mass inflow

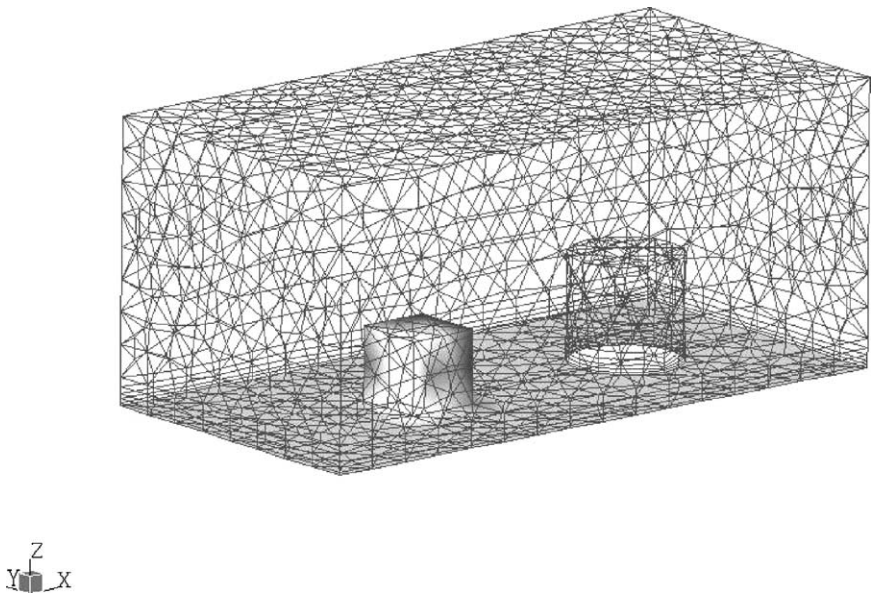

Fig. 4. Surface mesh of trial no. 29 computational domain. Air inflow from the left-hand side.

Table 1
Values of released gas inflow rate (m_i)

Trial number	Released gaseous mixture density relative to air	Total released volume (m^3)	Total released mass (kg)	Mass inflow rate, m_i ($kg\,s^{-1}$)
26	2.00	1970	4767	3178
29	2.00	1950	4719	3146

rate (Q_i) was given through a properly adapted step function [22]:

$$Q_i = m_i \times \text{step}\left[-\frac{(t-t_0)(t-t_1)}{t_c^2}\right] \quad (5.1)$$

where m_i takes the values given in Table 1.

5.2. Wind inlet

Wind speed is one of the most significant parameters in problem definition procedure, since it determines how quickly emitted gas will be diluted by passing volumes of air. The corresponding boundary condition should take into account the reduction of wind speed value near the ground level due to frictional effects.

If wind speed at a fixed height is known (typical reference height 10 m), then wind velocity profile may be given through a power low correlation

$$u_z = u_0 \times \left(\frac{Z}{Z_0}\right)^{\lambda} \quad (5.2)$$

where λ is a dimensionless parameter, whose value depends upon atmospheric stability category and surface roughness [23]. Regarding the trial nos. 26 and 29, the values of λ are given in Table 2.

In addition to the above, the ground and the building faces were defined as fixed stable walls, where the fluid velocity is equal to zero according to the non-slip condition, whereas the remaining planes of the domain were specified via a relative pressure value, which was set equal to zero and corresponds to the relative static pressure when outflow takes place.

6. Simulation results

Having determined the boundary conditions regarding trial nos. 26 and 29, mass, energy and momentum equations

Table 2
Values of parameter λ in power law correlation (Eq. (5.2))

Trial number	Wind speed at 10 m altitude ($m\,s^{-1}$)	Atmospheric stability	Surface roughness (m)	Parameter λ (unitless)
26	1.9	B	0.005	0.07
29	5.6	D	0.005	0.15

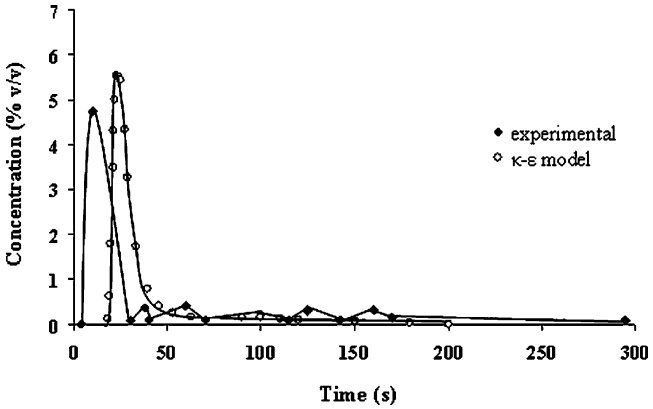

Fig. 5. Gas concentration vs. time for trial no. 26 (front face of building) using the k–ε turbulence model.

were solved in the 3D space limited by the domain boundaries. Computational grids consisted of 33,791 and 25,586 volume elements, respectively. Since the aim was to compute concentration values at different times, the problem must be solved in transient form. Total simulation time was 250 s for trial no. 26 and 90 s for trial no. 29 with relatively short time steps: 124 s ($8\times0.25\,s+20\times0.5\,s+60\times1\,s+36\times5\,s$) and 76 s ($8\times0.25\,s+40\times0.5\,s+3\times1\,s+20\times2\,s+5\times5\,s$), respectively. In both cases, each problem was firstly solved in steady state to obtain initial values for the transient simulations.

Steady state runs terminated after approximately 140–200 iterations allowing a reasonable convergence to be achieved. The convergence criterion was the residual RMS (residual of root mean square) to be equal to or less than 10^{-4}. Transient runs needed 7–12 iterations per time step to reach the desirable residual value. Total time required for the full simulation of a problem was fluctuated between three and eight hours on an 800 MHz Intel® Celeron processor with 256 MB of RAM, depending on the total number of time steps and the robustness of the turbulence model used.

Results obtained from the numerical simulation of trial 26 are shown in Figs. 5–12. In Figs. 5–8 computational re-

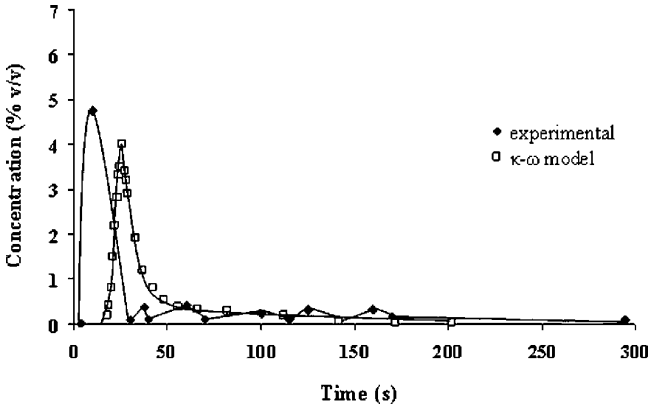

Fig. 6. Gas concentration vs. time for trial no. 26 (front face of building) using the k–ω turbulence model.

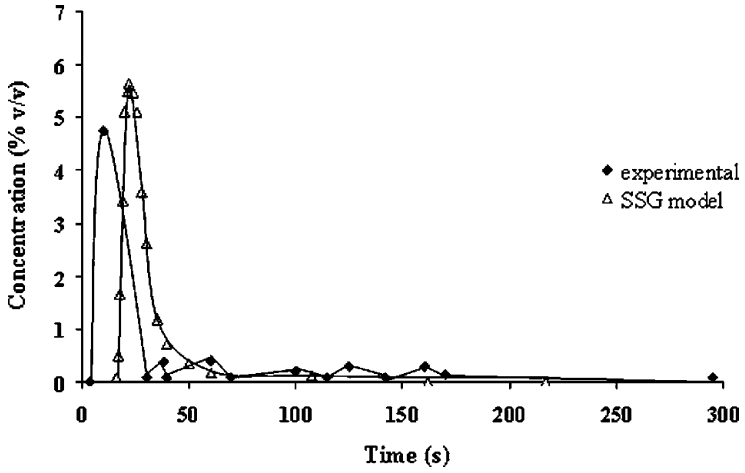

Fig. 7. Gas concentration vs. time for trial no. 26 (front face of building) using the SSG turbulence model.

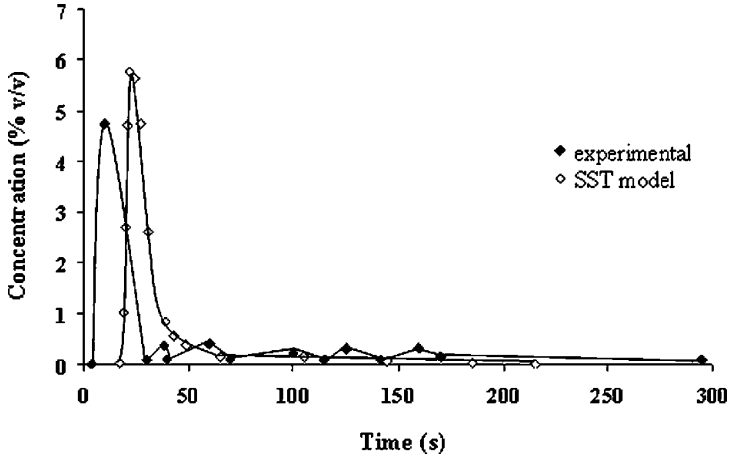

Fig. 8. Gas concentration vs. time for trial no. 26 (front face of building) using the SST turbulence model.

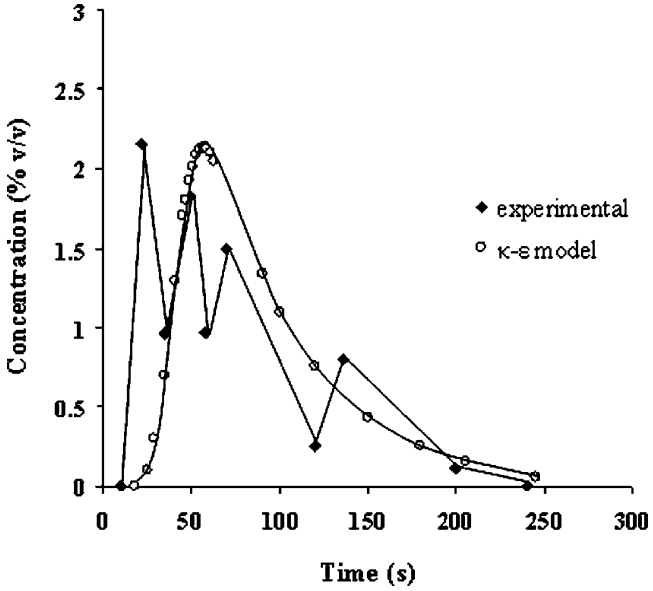

Fig. 9. Gas concentration vs. time for trial no. 26 (rear face of building) using the k–ε turbulence model.

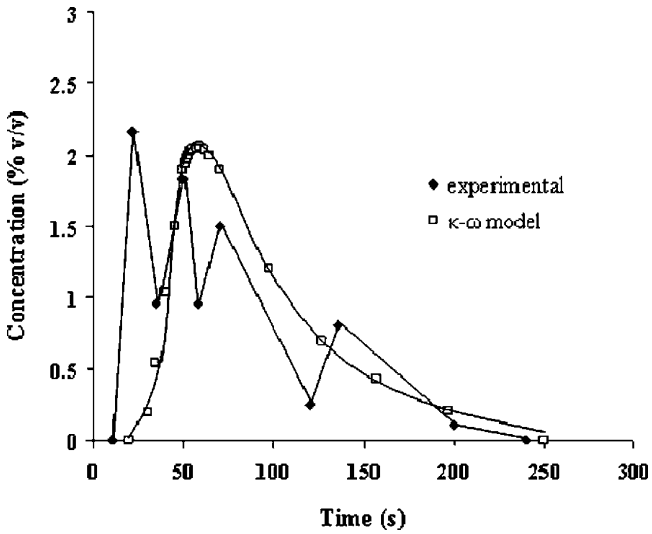

Fig. 10. Gas concentration vs. time for trial no. 26 (rear face of building) using the k–ω turbulence model.

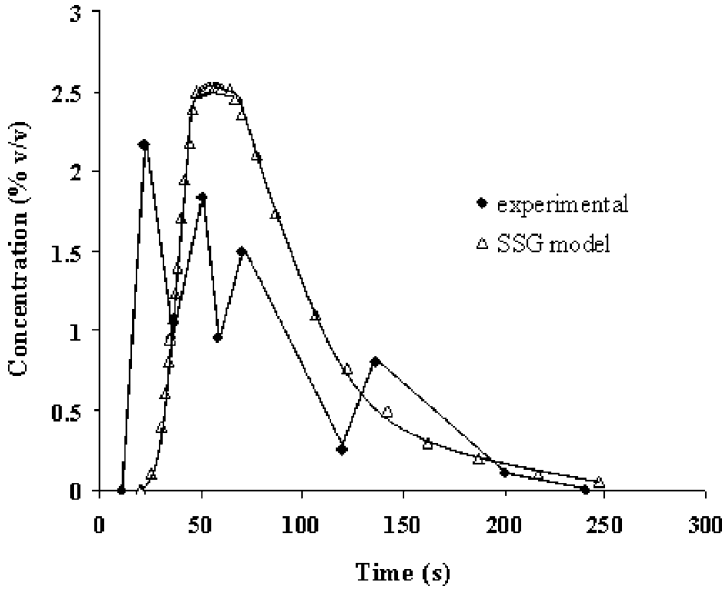

Fig. 11. Gas concentration vs. time for trial no. 26 (rear face of building) using the SSG turbulence model.

sults are compared with experimental concentration measurements recorded on the front face of building at the height of 6.4 m. In Figs. 9–12 results are compared with measurements recorded at the back face of building at the height of 0.4 m. As one can see, simulations yielded results that are found in good agreement with the experimental records. The difference between computed and experimental concentration curves lies in temporal hysteresis of the former considering the maximal concentration value.

With reference to trial no. 29, experimental data have been recorded to the back face of building at the height of 0.4 m. Their comparison with computational results is displayed in Figs. 13–16. In contrast with trial no. 26, computed concentration curves have a temporal antecedence compared with

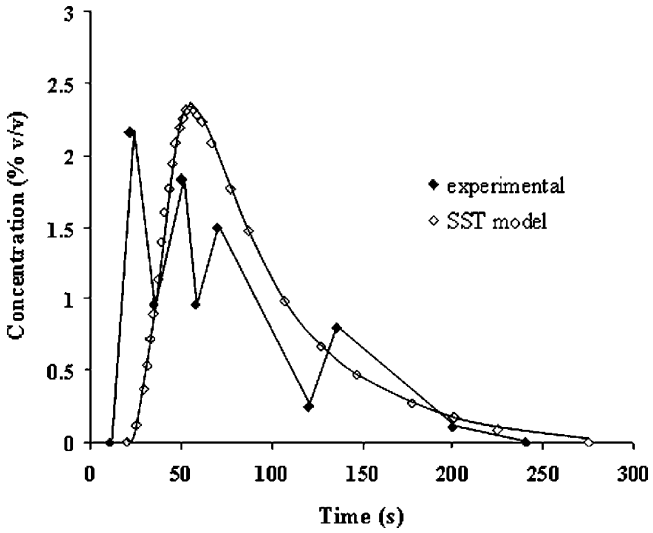

Fig. 12. Gas concentration vs. time for trial no. 26 (rear face of building) using the SST turbulence model.

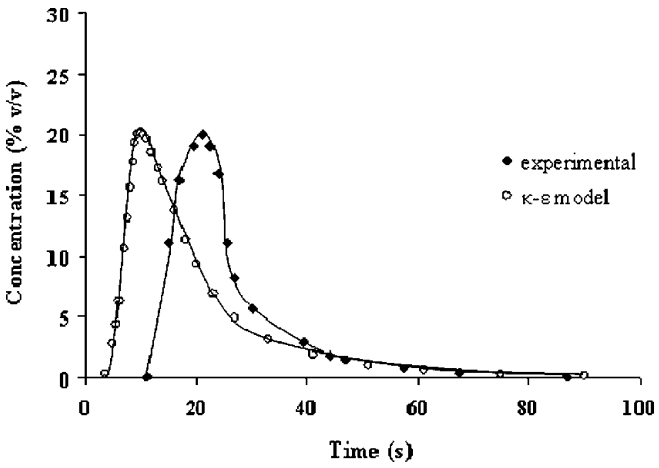

Fig. 13. Gas concentration vs. time for trial no. 29 (rear face of building) using the k–ε turbulence model.

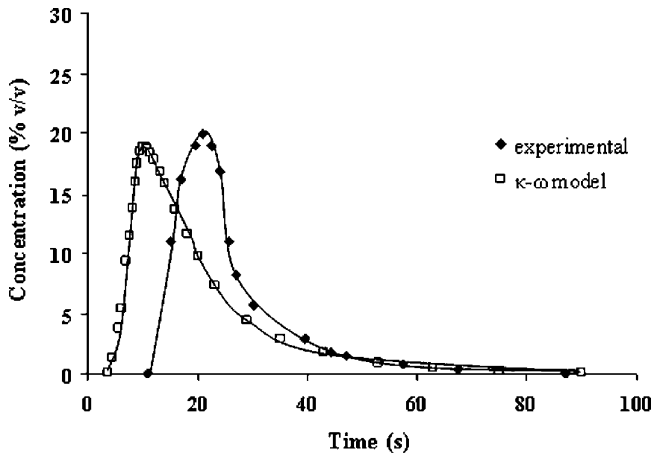

Fig. 14. Gas concentration vs. time for trial no. 29 (rear face of building) using the k–ω turbulence model.

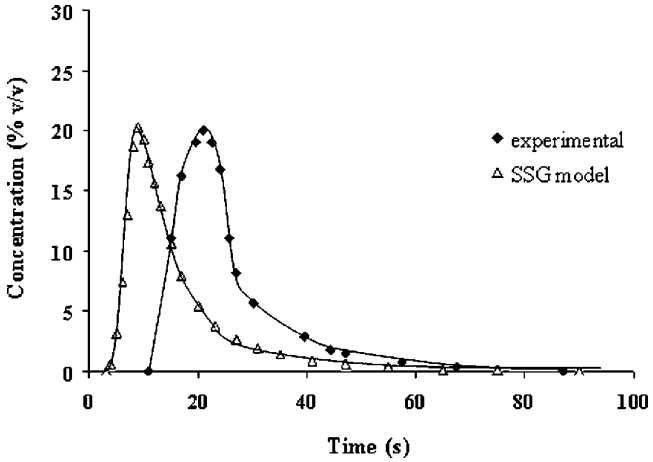

Fig. 15. Gas concentration vs. time for trial no. 29 (rear face of building) using the SSG turbulence model.

the experimental ones. Predicted maximal concentrations are found close to the experimental values with reasonable deviations.

Computed concentration curves for both trials appear to be smooth in comparison with experimental ones, due to the averaging process, which smoothes the fluctuations of computational data [24].

In general, CFD predictions were found to be in good agreement with experimental data. Among the models used in the simulations, k–ε and SST are distinguished for their robustness. They converged to the desired criterion (RMS $= 10^{-4}$) in a comparatively small number of iterations. Moreover, k–ε and SST models yielded results of good accuracy similar to that of SSG model, which however required perceptibly more CPU time to finish the calculations execution. The behavior of k–ω in the simulations was similar to that of k–ε model with slightly more requirements in CPU time and yielded results at about the same accuracy level as those of k–ε model (Tables 3 and 4).

That behavior of the models tested (overestimation as regards SSG, k–ε and SST and underestimation with reference to k–ω) is expressed through the systematic errors apparent through the plots and can be explained by the different turbulence parameters used in each model and hence, the different modifications in governing RANS equations. Perhaps, predicted maxima discrepancies, as well as temporal deviations regarding cloud arrival times would be diminished by using a much more refined mesh, but such an approach would demand large processing times and additional computational power.

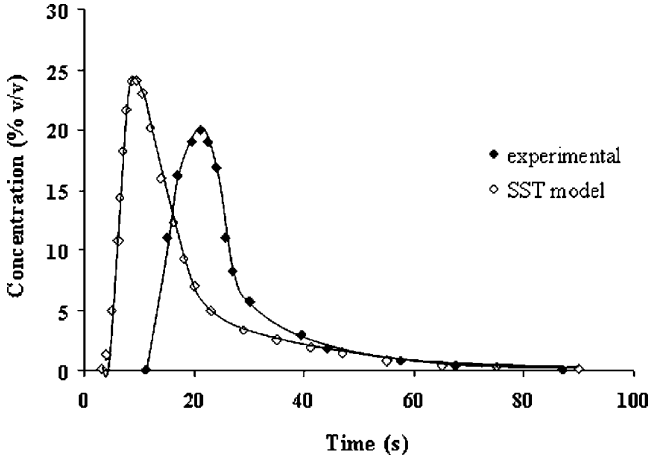

Fig. 16. Gas concentration vs. time for trial no. 29 (front face of building) using the SST turbulence model.

Table 3
Correction factors for experimental maximal concentrations

Condition	k–ε model	k–ω model	SSG model	SST model
Downwind correction factor	0.93	1.11	0.85	0.88
Upwind correction factor	0.99	1.06	0.99	0.83

Concerning the deviations that appear in Figs. 5–16 between computational and experimental concentration curves, appropriate factors may be established for the correction of the maximal concentration and the arrival time values predicted by the models. As referred in the work of Duijm et al. [25], assessment of dispersion modeling performance depends substantially on the data sets used. As a result, the correction factors calculated below will hardly be realistic for other experiments. If π is the experimental (true) value of concentration or the arrival time and υ the corresponding computational prediction (approximating value), then the correction factor (CF) is given by the relation

$$\mathrm{CF} = \frac{\pi}{\upsilon} \tag{6.1}$$

Maximal concentration correction factors are shown in Table 3, while the correction factors of arrival time are given in Table 4. Trial nos. 26 and 29 have opposite release orientation (downwind and upwind release) and, as a result, they should be considered separately in CF calculations.

Correction factors displayed in Tables 3 and 4 are the average CF values corresponding to a certain variable (maximal concentration and arrival time, respectively) and condition (downwind or upwind release). Correction factors displayed in Table 3 show that, independent of release conditions, k–ω model underestimates maximal concentrations, whereas k–ε, SSG and SST models overestimate them. In Table 4, as regards trial no. 26, downwind correction factors are smaller than unity indicating that arrival time is overestimated and hence computational concentration curves will present temporal hysteresis (Figs. 5–12). On the contrary,

Table 4
Correction factors for gas cloud arrival times at downwind and upwind conditions

Release conditions	k–ε model	k–ω model	SSG model	SST model
Downwind correction factor	0.49	0.43	0.47	0.48
Upwind correction factor	2.08	2	2.33	2.22

upwind correction factors corresponding to trial no. 29 are bigger than unity confirming computational underestimation of the arrival time, which leads to temporal precedence of computed concentration curves in Figs. 13–16.

Furthermore, it is evident from Figs. 5–16 that the experimental variability is very significant, whereas the experimental maxima are obtained from single point measurements. Consequently, the deviations between the experimental and the computed results may not be as great as they seem to be in some cases. Thus, it is quite probable that higher precision sensors could give results much closer to the computed ones.

7. Conclusions

Successful simulation of atmospheric gas dispersion contributes to a better comprehension of complex phenomena that dominate within the flow field under real conditions (presence of obstacles, turbulence generation). CFD codes constitute powerful tools in complex physical processes simulation providing high accuracy results with excellent visualization capabilities, which can be helpful in quantitative risk analysis applications.

The k–ε and SST models showed improved robustness during solver processing. The SSG model entailed increased CPU time without significant enhancement of accuracy of results. The SSG, k–ε and SST models appeared to overestimate maximal concentrations recorded in the trials, whereas k–ω model underestimate them.

In general, the results obtained through the numerical simulation show good agreement compared with the experimental data leading to the conclusion that computational fluid dynamics can be effectively used in toxic dispersion consequence assessment procedures, where “box” models have limited capabilities.

Acknowledgements

This work was supported by the Ministry of National Education and Religious Affairs (Community Support Framework 2000–2006) under the HERACLITUS research program.

References

[1] F. Rigas, S. Sklavounos, Risk and consequence analyses of hazardous chemicals in marshalling yards and warehouses at Ikonio/Piraeus harbour, Greece, J. Loss Prevent. Process Ind. 15 (2002) 531–544.
[2] F. Rigas, M. Konstandinidou, P. Centola, G.T. Reggio, Safety analysis and risk assessment in a new pesticide production line, J. Loss Prevent. Process Ind. 16 (2003) 103–109.
[3] F.P. Lees, Loss Prevention in the Process Industry, 2nd ed., Butterworths/Heinemann, Oxford, 1996, pp. 15 and 167.
[4] M.A. McBride, A.B. Reeves, M.D. Vanderheyden, C.J. Lea, X.X. Zhou, Use of advanced techniques to model the dispersion of chlorine in complex terrain, Process Safety Environ. 79 (2001) 89–102.
[5] G.A. Perdikaris, F. Mayinger, Numerical simulation of heavy gas cloud dispersion within topographically complex terrain, J. Loss Prevent. Process Ind. 7 (1994) 391–396.
[6] M.E. Davies, S. Singh, The phase II trials: a data set on the effect of obstructions, J. Hazard. Mater. 11 (1985) 301–323.
[7] J.W. Rottman, J.E. Simpson, J.C.R. Hunt, R.E. Britter, Unsteady gravity current flows over obstacles: some observations and analysis related to the phase II trials, J. Hazard. Mater. 11 (1985) 325–340.
[8] P.W.M. Brighton, A user’s critique of the Thorney Island dataset, J. Hazard. Mater. 16 (1987) 457–500.
[9] M. Nielsen, Dense gas field experiments with obstacles, J. Loss Prevent. Process Ind. 4 (1991) 29–34.
[10] T.O. Spicer, J.A. Havens, Field test validation of the DEGADIS model, J. Hazard. Mater. 16 (1987) 231–245.
[11] A.G. Venetsanos, J.G. Bartzis, J. Wurtz, D.D. Papailiou, DISPLAY-2: a two-dimensional shallow layer model for dense gas dispersion including complex features, J. Hazard. Mater. A 99 (2003) 111–144.
[12] J. Wurtz, J. Bartzis, A. Venetsanos, S. Andronopoulos, J. Statharas, R. Nijsing, A dense vapour dispersion code package for applications in the chemical and process industry, J. Hazard. Mater. 46 (1996) 273–284.
[13] S. Banerjee, R. Martini, M.J. Pattison, CLOUD: a vapour–aerosol dispersion model accounting for plume 3D motion and heat and mass transfer between phases, J. Hazard. Mater. 46 (1996) 231–240.
[14] J.C.F. Pereira, X.-Q. Chen, Numerical calculations of unsteady heavy gas dispersion, J. Hazard. Mater. 46 (1996) 253–272.
[15] C.A.J. Fletcher, Computational Techniques for Fluid Dynamics, Springer-Verlag, Berlin, 1997, pp. 47 and 105–111.
[16] CCPS, Understanding Atmospheric Dispersion of Accidental Releases, AIChE, New York, 1995, pp. 6–8 and 35.
[17] H.K. Versteeg, W. Malalasekera, An Introduction to Computational Fluid Dynamics—The Finite Volume Method, Longman, New York, 1995, pp. 49–53.
[18] ANSYS Company, CFX-5 Solver Theory Manual CFX Ltd., Oxfordshire, 2003, pp. 57–96.
[19] T.J. Chung, Computational Fluid Dynamics, Cambridge University Press, Cambridge, 2002, pp. 679–718.
[20] J. McQuaid, B. Roebuck, Large scale field trials on dense vapour dispersion, Report No. EUR 10029 (EN), 1985, pp. 200–204 and 262–267.
[21] D.M. Deaves, Three-dimensional model predictions for the upwind building trial of Thorney Island phase II, J. Hazard. Mater. 11 (1985) 341–346.
[22] R.G. Rice, D.D. Do, Applied Mathematics and Modelling for Chemical Engineers, Wiley, New York, 1995, pp. 361–363.
[23] CCPS, Consequence Analysis of Chemical Releases, AIChE, New York, 1999, pp. 80–83.
[24] J.S. Puttock, G.W. Colenbrander, Thorney Island data and dispersion modelling, J. Hazard. Mater. 11 (1985) 381–397.
[25] N.J. Duijm, S. Ott, M. Nielsen, An evaluation of validation procedures and test parameters for dense gas dispersion models, J. Loss Prevent. Process Ind. 9 (1996) 323–338.